Atmos. Chem. Phys. Discuss., 9, 8035–8069, 2009
www.atmos-chem-phys-discuss.net/9/8035/2009/

Atmospheric Chemistry and Physics Discussions

This discussion paper is/has been under review for the journal *Atmospheric Chemistry and Physics (ACP)*. Please refer to the corresponding final paper in *ACP* if available.

Global distributions of nitric acid from IASI/MetOP measurements

C. Wespes[1], D. Hurtmans[1], C. Clerbaux[2,1], M. L. Santee[3], R. V. Martin[4,5], and P. F. Coheur[1]

[1]Spectroscopie de l'Atmosphère, Chimie Quantique et Photophysique, Université Libre de Bruxelles (U.L.B.), Brussels, Belgium
[2]UPMC Univ. Paris 06, CNRS UMR8190, LATMOS/IPSL, Paris, France
[3]Jet Propulsion Laboratory, California Institute of Technology, Pasadena, California, USA
[4]Department of Physics and Atmospheric Science, Dalhousie University Halifax, Canada
[5]Harvard-Smithsonian Center for Astrophysics, Cambridge, Massachusetts, USA

Received: 29 January 2009 – Accepted: 28 February 2009 – Published: 25 March 2009

Correspondence to: C. Wespes (cwespes@ulb.ac.be)

Published by Copernicus Publications on behalf of the European Geosciences Union.

Abstract

This paper presents the first global distributions of HNO_3 acquired by the Infrared Atmospheric Sounding Interferometer (IASI) instrument, launched onboard the MetOp platform in October 2006. IASI is an infrared nadir-looking Fourier transform spectrometer providing atmospheric radiance spectra at 0.5 cm^{-1} spectral resolution, from which temperature and infrared absorbing gas concentration profiles are retrieved with global Earth coverage twice a day. A first analysis of the IASI measurements in terms of information content demonstrates the possibility of retrieving a total column for HNO_3 at all latitudes with a maximal sensitivity in the middle stratosphere. The retrievals are performed from IASI spectra in the atmospheric window using a fast radiative transfer model and inversion software relying on the Optimal Estimation Method. The operational processing of HNO_3 is achieved since March 2008. The global distributions of the retrieved total columns for 10 months (from March to December 2008) are presented and discussed with emphasis given to seasonal and interhemispheric variations. Local trends at 6 specific locations are also described and discussed in comparison with MLS volume mixing ratios at 46.5 hPa. The seasonal cycle observed in Polar regions is highlighted, with maxima observed in fall and minima during spring-summer. The denitrification inside the Antarctic polar vortex during winter is clearly revealed with unprecedented horizontal resolution: HNO_3 columns decreasing down to about 1×10^{16} molecules.cm^{-2} are observed, which is consistent with the lower values of temperature observed between 50 and 15 hPa (~20–25 km) and the resulting formation and sedimentation of polar stratospheric clouds. During the same period, the collar region of high quantities of HNO_3 at the vortex edge is also observed around 65–60° S latitude. Preliminary correlations between IASI derived HNO_3 and O_3 columns inside the polar vortex are presented and discussed.

1 Introduction

HNO_3 is the dominant form of oxidized nitrogen in the atmosphere, usually abbreviated as NO_y (NO_y=NO_x+oxidized products, with NO_x=NO+NO_2). It is an important reservoir and sink species for NO_x in both the troposphere and the stratosphere and as such is a key component for the understanding of the chemical processes in the lower atmosphere (Solomon, 1999; Brasseur and Solomon, 2005). Deposition of HNO_3 at the surface in the form of acid rain is a threat for the environment and contributes to the acidification of soils and water. Nitric acid is mainly present in the stratosphere, with only a small fraction (about 5%) in the troposphere. In the stratosphere, it contributes, along with other oxidized forms, in sequestering NO_x, thereby reducing catalytic ozone destruction processes (Solomon, 1999; Brasseur and Solomon, 2005). It is removed from this layer either by photochemistry or by sedimentation of Polar Stratospheric Cloud (PSC) particles containing HNO_3 during the cold polar nights. This process causing stratospheric denitrification also influences chlorine chemistry and is an important factor governing the ozone hole development in polar springtime (Solomon, 1999; Santee et al., 1999, 2004; Jin et al., 2006, and references therein).

In the troposphere, HNO_3 is the dominant sink of NO_x. Its role as a reservoir species involved in long-range transport of NO_x pollution is, however, not excluded (Hauglustaine et al., 1998; Emmons et al., 2000; Bey et al., 2001; Neuman et al., 2006). Nitrate aerosols formed from HNO_3 in the troposphere are also of increasing importance for climate (Adams et al., 2001).

Until recently, HNO_3 observations were restricted to local measurements in the troposphere, for example during airborne campaigns (Emmons et al., 2000, and references therein; Miyazaki et al., 2003; Hudman et al., 2004), or to extensive satellite measurements in the stratosphere and in the upper troposphere. Global distributions of HNO_3 in the stratosphere have been obtained from a series of limb-sounders operating in the infrared (IR) or millimeter spectral range by averaging over time. These have highlighted spatial, seasonal and inter-annual variations (Koike et al., 2000; Irie

ACPD
9, 8035–8069, 2009

et al., 2002, 2006; Santee et al., 1999, 2004, 2005, 2007; Urban et al., 2005; Tsidu et al., 2005; Stiller et al., 2005; Fisher et al., 2008; Wang et al., 2007). The longest and the most complete set of observations was recorded between 1991 and 1998 by the Microwave Limb Sounder (MLS) on board the Upper Atmosphere Research Satellite (UARS). These long term observations in the stratosphere are complemented by the Odin Sub-Millimetre Radiometer (SMR) since 2001, by MLS on the Aura satellite since 2004 (Santee et al., 2004, 2007; Urban et al., 2008), by the Michelson Interferometer for Passive Atmospheric Sounding (MIPAS) on Envisat platform (Tsidu et al., 2005; Stiller et al., 2005; Fisher et al., 2006; Wang et al., 2007) and the Atmospheric Chemistry Experiment Fourier Transform Spectrometer (ACE-FTS) infrared instrument (Bernath et al., 2005; Martin et al., 2006; Wolff et al., 2008). In the best cases, these limb-sounders enable sounding down to the upper troposphere but are limited for measuring NO_x pollution sources outflow and chemical transformation.

High resolution nadir infrared satellite measurements have very recently demonstrated their capability to assess global distributions of nitric acid partial columns in the troposphere and the stratosphere with a limited sensitivity to the vertical profiles (Wespes et al., 2007). These promising results were obtained by analyses of the Interferometric Monitor for Greenhouse gases instrument (IMG)/ADEOS, which provided measurements for 10 months in 1996–1997. It is the only global scale distribution available up to now. The Tropospheric Emission Spectrometer (TES)/Aura (Beer et al., 2006) does indeed not routinely probe the nitric acid absorption spectral range around $900\,cm^{-1}$, and from the Atmospheric Infrared Sounder (AIRS) on Aqua, near-real time measurements of HNO_3 are achieved, but to the best of our knowledge, no geophysical studies of the resulting fields have been performed.

The Infrared Atmospheric Sounding Interferometer (IASI) satellite launched onboard the MetOp platform is a relatively high spectral resolution IR sounder, covering an extended spectral range with a very low radiometric noise. Owing to its spatial and temporal coverage, the IASI mission is providing global measurements of accurate temperature and atmospheric abundances for about 10 species twice a day, with small ground

pixel size (Clerbaux et al., 2009). As MetOp is an operational satellite, near real time global distributions of HNO_3 can be measured in the lower stratosphere, and column measurements from IASI have been performed at the "Université Libre de Bruxelles" (ULB) since March 2008 using a dedicated fast radiative transfer model.

This paper shows the first results of 10 months of IASI processing, focusing on global distributions and seasonal variations. The total columns are dominated by the stratosphere, and the geophysical analysis is therefore oriented towards stratospheric chemistry, in particular over polar regions. In Sect. 2, the characteristics of IASI measurements and the retrieval method are described. In Sect. 3, we briefly discuss the vertical sensitivity and errors of the measurements. We then present the global distributions of HNO_3 total columns and we discuss the spatial and temporal variations, with particular focus on polar regions.

2 Measurements and methods

2.1 IASI measurements

The IASI remote sensor was launched onboard the MetOp sun-synchronous polar orbiting meteorological platform on 19 October 2006 (Clerbaux et al., 2007, 2009). The IASI instrument is a high resolution nadir-viewing Fourier transform spectrometer characterized by an apodized spectral resolution of $0.5\,cm^{-1}$ and a $0.25\,cm^{-1}$ spectral sampling. It is designed primarily to measure temperature and water vapor profiles with high accuracy and vertical resolution in the troposphere to benefit atmospheric weather prediction. IASI measures the thermal infrared emission emitted by the Earth-atmosphere system between 645 and $2760\,cm^{-1}$ with a field of view of 2×2 circular pixels on the ground, each of 12 km diameter at nadir. The spectra have low radiometric noise (between 1.2×10^{-7} W/(cm^2.sr.m^{-1}) around $2200\,cm^{-1}$ and 2.2×10^{-6} W/(cm^2.sr.m^{-1}) around $750\,cm^{-1}$), allowing the simultaneous detection and monitoring of several IR absorbing species (Coheur et al., 2009; Boynard et al., 2009;

ACPD
9, 8035–8069, 2009

Clarisse et al., 2009; George et al., 2009; Razavi et al., 2009; Turquety et al., 2009). The IASI measurements are taken at nadir every 50 km along the trace of the satellite. Measurements are also taken across-track over a swath width of 2200 km. Because of its high temporal sampling, IASI provides global coverage of the Earth twice daily. It is programmed for a period of 15 years with three successive launches.

2.2 Radiative transfer model

In order to handle the large IASI data flow, a fast radiative transfer model has been developed specifically for HNO_3, the FORLI-HNO_3 (Fast Operational/Optimal Retrievals on Layers for IASI) software. This software differs significantly from the Atmosphit software (e.g. Barret et al., 2005; Coheur et al., 2005), used in previous HNO_3 retrievals from IMG (Wespes et al., 2007) and on a case basis for the present work (Sect. 3.1.). FORLI-HNO_3 differs mainly from Atmosphit in that it relies on look-up tables of pre-calculated absorption cross sections at varying pressures and temperatures. Such Look-Up Tables (LUTs) have only been constructed for HNO_3 and H_2O because of the absence of other strong absorbers in the spectral window of interest (see the following section). These tables have been pre-computed from 810 to 960 cm^{-1} using line parameters from the HITRAN database (Rothman et al., 2005) on a logarithmic grid in pressure and a linear grid in temperature and in humidity (for water vapour lines). In order to accurately represent the atmospheric state at each location on the globe, lower and upper limits are respectively set to 162.8 K and 322.64 K for temperature and to −10 and 0 for the logarithm of pressure (4.5×10^{-5} to 1 atm) with a grid step of 5 K for temperature and 0.2 for the logarithm of pressure. For water vapour, a third dimension is brought to the grid by considering relative humidity between 0 and 100 and a step of 10. LUTs have been constructed with a spectral sampling of 0.025 cm^{-1} (oversampling of 10 vs. the 0.25 cm^{-1} spectral sampling of IASI).

The direct computations of the IASI spectra are then calculated from the LUTs for each location using detailed radiative transfer simulations. The absorbance spectra are convolved with the IASI instrumental line shape, represented by a Gaussian function

with 0.5 cm^{-1} full width at half maximum and then set on the 0.25 cm^{-1} spectral sampling grid. The relationship between the measured radiances (measurement vector), $\boldsymbol{y}$, and the true atmospheric state (state vector), $\boldsymbol{x}$, is given by $\boldsymbol{y}=\mathbf{F}(\boldsymbol{x},\boldsymbol{b})+\varepsilon$ where $\mathbf{F}$ is the forward radiative transfer function, $\boldsymbol{b}$ represents model parameters affecting the measurement and ε is the measurement noise. The radiative transfer function represents the radiance originating from Earth surface, attenuated after passing through the atmosphere, also including the contribution of the average downward flux reflected by the Earth's surface. The radiative transfer calculations use as input the temperature, pressure and humidity profiles provided by EUMETSAT from the operational processing of MetOp sounding observations (Schlüssel et al., 2005). In order to provide the best match with the observations, both the surface temperature and the humidity profiles are included in the state vector for the retrieval step, as discussed in the following section. Importantly, only cloud-free scenes are considered. The cloud information from the operational processing is used for filtering the observations, and only scenes with cloud coverage below 25% are analyzed.

2.3 Retrieval method and settings

The retrieval of a concentration profile from nadir observations is an ill-conditioned problem that needs to be constrained to provide meaningful results. The retrieval scheme used here the formalism of the Optimal Estimation Method (OEM) (Rodgers, 2000). Following the latter, an approximation $\hat{\boldsymbol{x}}$ of the true state $\boldsymbol{x}$ (usually a vertical concentration profile) is retrieved from IASI observations using, on one hand, the measurement vector $\boldsymbol{y}$ (here, the IASI radiances) and the associated noise variance-covariance matrix, $\mathbf{S}_{\varepsilon}$, and, on the other hand, a priori information on concentration for the species to be retrieved. The prior information consists of an a priori profile $\boldsymbol{x}_a$ and a variance-covariance matrix, $\mathbf{S}_{\mathbf{a}}$, that should ideally represent the true variability of the target species in space and time. For a non-linear problem, the retrieved state, $\hat{\boldsymbol{x}}$, is found by iteration of: $\hat{\boldsymbol{x}}_{i+1}=\boldsymbol{x}_a+(\mathbf{K}_i^T\mathbf{S}_{\varepsilon}^{-1}\mathbf{K}_i+\mathbf{S}_{\mathbf{a}}^{-1})^{-1}\mathbf{K}_i^T\mathbf{S}_{\varepsilon}^{-1}\left[\boldsymbol{y}-\mathbf{F}(\hat{\boldsymbol{x}}_i)+\mathbf{K}_i(\hat{\boldsymbol{x}}_i-\boldsymbol{x}_a)\right]$ where

$\mathbf{K}_i=(\partial\mathbf{F}(\hat{x})/\partial x)_i$ represents the Jacobian matrix. It is computed analytically. The error covariance of the solution is given by $\hat{\mathbf{S}}_{i+1}=\left(\mathbf{K}_{i+1}^T\mathbf{S}_\varepsilon{}^{-1}\mathbf{K}_{i+1}+\mathbf{S}_\mathbf{a}^{-1}\right)^{-1}$. The solution is reached when the absolute difference between every element of $\mathbf{F}$ modeled at two successive iteration steps, $|\mathbf{F}(\hat{x}_{i+1})-\mathbf{F}(\hat{x}_i)|$, is less than a fraction (20%) of the measurement noise. The logarithmic space has been chosen during the iterative process in order to avoid negative concentrations.

For the retrievals, a wide spectral window extending from 860 to 900 cm^{-1} that encompasses the ν_5 and $2\nu_9$ absorption bands of HNO_3 is selected. Although these bands are not the most intense absorption features of HNO_3 in the thermal infrared, the choice is justified by limited strong overlapping other trace gases absorption features in this spectral region. As in previous studies, we consider here a diagonal noise covariance matrix, $\mathbf{S}_\varepsilon=\sigma_\varepsilon^2\mathbf{I}$, with a value $\sigma_\varepsilon=2\times10^{-6}$ W/(cm^2.sr.m^{-1}) close to the expected IASI noise. Similarly, a single HNO_3 a priori profile (see Fig. 1) is used: it is built from a set of composite measured and modeled profiles in such a way as to represent a global and annual mean HNO_3 profile in the troposphere and the stratosphere. The model profiles from LMDZ-INCA (Hauglustaine et al., 2004) on a 3.75° longitude × 2.50° latitude grid over one year have been considered to capture tropospheric variability up to 15.6 km. For the stratosphere up to 60 km, highly resolved vertical profiles measured by the ACE-FTS occultation sounder (Boone et al., 2005) over more than 2 years have been used. The suitable model and measured profiles were resampled on vertical scales and combined to provide an ensemble of profiles from which the mean was computed. For the operational processing, only a total HNO_3 column is retrieved. It has been performed by using a global profile scaling. The choice of retrieving a total column rather than a profile is justified by the absence of vertical sensitivity, as will be discussed in Sect. 3.1.

For the total column retrieval, a variance-covariance S_a=100% has been considered. In addition to the HNO_3 total column, the state vector includes surface temperature and water vapour profiles from the ground to 19 km. The retrieval settings are summarized

in Table 1. The retrieved HNO_3 product consists of a total column and an associated error computed as $\hat{x}-x=(\hat{S})^{\frac{1}{2}}$ when convergence is reached. It includes contributions from the measurement noise, from the limited vertical sensitivity of the measurement, and from the errors on fitted model parameters.

2.4 Posteriori filtering

A posteriori filtering of the data was necessary to remove some strongly biased HNO_3 columns. First, extremely noisy spectra were removed based on the root mean square values of the spectral residuals after the retrievals. Furthermore, we have found that some emissivity features in IASI spectra over deserts, likely associated with calcite, cause an overestimation of the HNO_3 total columns. A post-filtering of these scenes has also been performed. Finally, in order to exclude measurements with weak sensitivity to the HNO_3 total column, we have also removed data characterized by a total error greater than a fraction (32%) of HNO_3 total column.

3 Results and discussion

3.1 Vertical sensitivity and errors

In order to evaluate the methodology of the FORLI-HNO_3 processing described above and in particular the choice of adjusting only a total column of HNO_3, we have performed a series of full profile retrievals at representative latitudes using the line-by-line Atmosphit software described elsewhere (Barret et al., 2005; Coheur et al., 2005). Relying on the OEM for the retrieval part, it provides as output all parameters needed for characterizing the retrieved state in terms of vertical sensitivity. The vertical sensitivity is analyzed by means of the averaging kernel matrix: $\mathbf{A}=\partial\hat{\boldsymbol{x}}/\partial\boldsymbol{x}=(\mathbf{K}^T\mathbf{S}_{\varepsilon}^{-1}\mathbf{K}+\mathbf{S}_{\mathbf{a}}^{-1})^{-1}\mathbf{K}^T\mathbf{S}_{\varepsilon}^{-1}\mathbf{K}$, the rows of which provide an estimation of the altitude of maximum sensitivity (the peak of the function) and of the vertical resolution

ACPD
9, 8035–8069, 2009

(their full width at half maximum). The number of independent pieces of information in the retrieved profiles is calculated as DOFS=trace(**A**).

For the purpose of the characterization, profiles are retrieved on 9 levels, extending from the ground to 40 km. The a priori profile shown in Fig. 1 is used here in combination with the full covariance matrix built from the ensemble of profiles, $\mathbf{S_a}$. The resulting a priori variability is maximum at ground level with about 170% variability, reduces to around 80% in the troposphere and the lower stratosphere, and strongly decreases down to 30% above 20 km in altitude.

Figure 2 shows a typical spectral fit in the selected retrieval window for a polar observation (Fig. 2a) where the amount of water vapor is low and the nitric acid absorption features are clearly identified. A good spectral adjustment is obtained, with a residual (observed-calculated) around the selected value of σ_ε (2×10^{-6}W/cm^2.sr.m^{-1}). The averaging kernels for the nine retrieval layers and for the total column are shown in Fig. 2b. They all present the same shape covering the entire altitude range from the troposphere to the stratosphere, in agreement with a DOFS of 1. This result points to the absence of vertical information for HNO_3 in the IASI measurements and justifies the retrieval of a total column. The analysis of the averaging kernels further reveals a maximum sensitivity in the lower stratosphere (approximately between 15 and 30 km) and a weaker sensitivity close to the surface, which is inherent to thermal IR sounding in the case of low thermal contrast (see Clerbaux et al., 2009, for a more complete discussion). These results hold at all latitudes, despite a slightly enhanced vertical sensitivity at tropical latitudes resulting from the higher surface temperatures. The absence of vertical sensitivity to the HNO_3 profile as compared to our previous work on IMG (Wespes et al., 2007) clearly points to the coarser spectral resolution of IASI (0.5 cm^{-1} as compared to 0.1 cm^{-1}) which does not sufficiently resolve the spectral lines.

The error on the retrieved HNO_3 total column is strongly variable on the globe, ranging from a few percent up to the threshold value of 32% (see previous section). We found higher errors at polar latitudes and in the equatorial belt. This can be explained by, on one hand, weaker sensitivity to HNO_3 measurements at the poles due to weaker

radiances and, on the other hand, by the impact of water vapor lines, which strongly interfere with HNO_3 features at the equator.

3.2 Global distributions

This section presents and discusses the results from the operational processing of IASI data using FORLI, to retrieve total column for HNO_3. Analysis of the IASI spectra after the cloud and posteriori filterings (on average 10–15% of IASI spectra are conserved) provides quasi-global distributions daily, with a horizontal resolution and temporal sampling never achieved before. In order to shed light on these small-scale variations, Fig. 3 presents HNO_3 total column distributions in the Southern Hemisphere for 3 successive days, with columns averaged on a $1^\circ \times 1^\circ$ grid. Obviously, the IASI concentration fields contain a wealth of information that will be useful to analyze local chemical and physical processes in Earth's low atmosphere. Such analyses have not yet been performed, and the remainder of this section focuses instead on large scale features that are better observed by averaging over several days.

As a first example, Fig. 4 shows the monthly evolution of the global distributions of HNO_3 from March 2008 to December 2008 in polar orthographic projections, for the Northern and Southern Hemispheres. For each month, the data are averaged on $1^\circ \times 1^\circ$ grid, only over a series of successive days (see Table 2), in order to highlight as much as possible the temporal dependence of HNO_3 abundances. The same set of days is not used for all months because of instrument sampling issues (data gaps). Figure 4 also shows two temperature isocontours of 195 K and 188 K (in blue lines) observed at 50 hPa, which are found in the range of altitude characterized by the maximal sensitivity of the measurements (see previous section). The 195 K and 188 K temperatures are found inside the polar vortex and correspond to the thresholds for type 1 and type 2 PSC formation, respectively. Values of potential vorticity (PV) at the potential temperature of 520 K (~50 hPa) gathered from the Met Office fields[1] for MLS

[1] online available at: https://mls.jpl.nasa.gov/dmp/

analyses have further been used to represent the size, the shape and the strength of the polar vortex and are superimposed as black lines in Fig. 4. As can be seen from Fig. 4, the IASI measurements capture the large scale variations of HNO_3 with latitude: low values characterized by a total column down to about 1×10^{16} molecules/cm^2 on average are found in the intertropical belt, progressively increasing towards polar regions, where they approach 4.5×10^{16} molecules.cm^{-2}. This behavior is observed for all seasons as will be discussed in greater detail below. The only exception to this gradient occurs in the Southern Hemisphere winter and spring (June to December), when denitrification inside the Antarctic polar vortex produces a strong decrease of the column down to 1×10^{16} molecules.cm^{-2}. The distributions shown in Fig. 4 reveal also large seasonal variability at the highest latitudes in both hemispheres, in constrast to the tropical and middle latitudes, where monthly variations are not observed. As a general rule, except in the PSC-formation regions, we find at high latitudes weaker concentrations in summer and higher abundances in winter and springtime. For example, the concentrations at chosen mid-latitude (Moshiri, 44° N, 142.3° E) and polar sites (Ny Alesund, 78.9° N, 11.9° E) in the Northern Hemisphere vary on average between 2.45×10^{16} molecules.cm^{-2} at the end of March to 1.35×10^{16} molecules.cm^{-2} in July and between 3.15×10^{16} molecules.cm^{-2} in March to 1.80×10^{16} molecules.cm^{-2} in July, respectively. These large-scale spatial and seasonal variations in the HNO_3 total columns are fully consistent with the photochemical processes occurring in the stratosphere (Austin et al., 1986; Rinsland et al., 1991; Santee at al., 1999, and references therein; Santee et al., 2004; Urban et al., 2008, among others). This result, which was anticipated from the vertical sensitivity analysis, points to a weak impact of the tropospheric HNO_3 component on the total column.

As already pointed out above, a remarkable pattern appearing in the spatial and monthly distributions of the HNO_3 total columns is the strong depression found inside the Southern Hemisphere polar vortex during winter and spring. During this period (June to October), the temperatures in the stratosphere are indeed cold enough to form PSCs of type 1 (from 195 K) and of type 2 (from 188 K). This causes local denitrification

inside the vortex and leads at the same time to a collar region of enhanced HNO_3 concentrations at and around the vortex edge. The strong depletion of HNO_3 starts in June when temperatures fall below the type 2 PSC threshold and reaches a maximum during July. The HNO_3-rich air region is found at and around the polar vortex, which is highlighted in Fig. 4 by contours of PV (black lines) at the potential temperature level of 520 K. During the period analyzed in this work, temperatures in the Arctic were not low enough to lead to denitrification.

In order to further illustrate the seasonal variations of the HNO_3 columns with latitude, Fig. 5 presents a time series of total columns from March to December 2008, with the IASI data gridded on 1 day×1°. A transition in total column values during July is observed, which corresponds to changes, in the forward model function, during this work. The isocontours of 195 K, 188 K for temperature at 50 and 15 hPa (~20 and 25 km) and three different values for potential vorticity are also shown. The hemispheric differences in the total columns already appearing from the zonal projections in Fig. 4 are highlighted, showing maxima around 4.5×10^{16} molecules.cm^{-2} during March in the Northern Hemisphere and around 5×10^{16} molecules.cm^{-2} during May in the Southern Hemisphere. These high values above Antarctica are found in the collar region at and around the vortex edge, as explained above. The temporal trend is in agreement with previous work reporting on the long-term evolution of global stratospheric distributions measured by UARS/MLS and Odin/SMR satellites (Santee et al., 2004; Urban et al., 2008). Figure 5 highlights again the fact that the distributions over the polar regions are governed by the strength and the spatial extent of the polar vortices as well as the lowest stratospheric temperatures, which control PSC formation. Interestingly, a closer look into this region of widespread denitrification reveals HNO_3 values markedly higher than expected at the end of August and which are persistent for several days in spite of the low temperature at 50 hPa (grey lines in Fig. 5). A possible explanation could be the warming of the stratosphere at higher altitudes (for example, isocontour of 188 K at 15 hPa shown as a white line on Fig. 5) well above the PSC formation thresholds, causing the PSC particles to evaporate and to release HNO_3 in the gas phase.

Figure 6 presents similar time series of HNO_3 total columns over the 10 months analyzed here, but for 1° latitude × 2° longitude grid boxes around six specific locations representative of polar (Fig. 6a and b), middle (Fig. 6c and d) and equatorial (Fig. 6e and f) latitudes in both Northern and Southern Hemispheres. The average temporal trend is given by the white curve, while the light grey area represents daily variations (3σ value of the standard deviation) in the spatial grid box. HNO_3 mixing ratios of MLS at the pressure level of 46.5 hPa measured at the same locations are superimposed for the purpose of comparison. A detailed description of the MLS HNO_3 level 2 products is provided by Froidevaux et al. (2006) and by Santee et al. (2007). As discussed above, the amplitude of the seasonal cycle is negligible at equatorial latitudes and becomes progressively stronger towards the poles. We note however a slight trend of the total columns at Reunion Island (Fig. 6f) which is not apparent at Mauna Loa (Fig. 6e). At middle latitudes, both in the Northern and in the Southern Hemispheres, higher values are found in the springtime and lower values during fall, with the amplitude of the seasonal cycles around 1×10^{16} molecules.cm^{-2}. These seasonal variations are partly masked by the extent of daily variability, with the 3σ value of the daily standard deviation in the grid box being twice as large as the amplitude of the seasonal variations. We also note a very different behavior between the Northern and the Southern polar latitudes. In the Arctic, the seasonal variations are strongly masked by the daily variations, which reach 3.5×10^{16} molecules.cm^{-2} (3σ), whereas in the Antarctic, the particular behavior of HNO_3 inside and around the polar vortex core is clearly visible. Overall, the trends of total columns are in agreement with those of MLS mixing ratios at 46.5 hPa in the stratosphere, emphasizing again the very dominant contribution of the stratospheric component to the IASI measured total column. The most remarkable gain of IASI as compared to limb sounders such as MLS lies in the number of measurements which allows monitoring the daily as well as the small-scale spatial variations. The comparisons with MLS constitute a good qualitative validation of IASI columns. A quantitative validation of the IASI measured total columns is not possible at this stage due to the absence of archived data from ground based measurements. We note, how-

ACPD
9, 8035–8069, 2009

ever, that the range of values reported here is consistent with extensive measurements made recently in the frame of MIPAS validation (Vigouroux et al., 2007).

3.3 Preliminary comparison with O_3 total columns

One of the strengths of the IASI mission for atmospheric chemistry lies in the simultaneous measurement of about 10 species with excellent horizontal resolution. Of particular relevance for HNO_3 chemistry in both the stratosphere and troposphere is the relationship with ozone. Figure 7 compares the Southern Hemispheric global distributions respectively of HNO_3 and O_3 total columns for two periods characterized by depletion of HNO_3. The IASI O_3 fields are also retrieved in a near real time mode, for a full description of the ozone product the reader should refer to Turquety et al. (2004) and Massart et al. (2009). Contours of potential vorticity and temperatures of PSC formation are superimposed on the maps, as in Fig. 4. The first illustrated period, 8–10 August 2008, is characterized by significant denitrification inside the polar vortex (see the previous section) but is prior to the ozone hole development. As a result, the HNO_3/O_3 ratios (top right panel in Fig. 7) are characterized by elevated values (about 5×10^{-3}) in the collar region circling the vortex and very low values (about 5×10^{-4}) inside the denitrified vortex core. During the second period in early spring, 9–15 September, the ozone hole is close to its maximum and both the HNO_3 and O_3 total columns inside the vortex show lower values. The resulting HNO_3/O_3 ratios (bottom right panel in Fig. 7) show somewhat less latitudinal variation (between 1×10^{-3} and 4×10^{-3}) than for the August period, even though the HNO_3 rich collar region remains still clearly apparent. Figure 8 shows the evolution of the HNO_3/O_3 ratios in 5° latitude bands from 50 to 85° S for the 10 months analyzed here. On a daily average basis, the ratio values vary between 1×10^{-3} and 4×10^{-3}. Minimum values are found during the denitrification period prior to the stratospheric ozone hole formation (see shaded blue area in Fig. 8) at lower latitudes. At the end of the polar night, the values of the ratio are increasing because of the ozone losses. For all latitudes, the temporal average trend in the HNO_3/O_3 ratios

is again weaker than the extent of daily variation. We also note that, except for the denitrification period, the HNO_3/O_3 ratio increases on average with latitude, pointing to the larger latitudinal gradient of HNO_3 as compared to that of ozone. The HNO_3/O_3 ratios obtained from IASI measurements are in agreement with previous studies which report values ranging from 1.8×10^{-3} to 9×10^{-3} in the lower stratosphere (Trainer et al., 1993; Bregman et al., 1995; Talbot et al., 1997; Schneider et al., 1999; Neuman et al., 2001).

4 Summary and conclusions

Nitric acid total columns have been retrieved globally from IASI measurements in a dedicated window (860–900 cm^{-1}) despite the weakness of the signal, but without any vertical information. The FORLI-HNO_3 (Fast Operationnal Retrievals on Layers for IASI) software, a fast radiative transfer model coupled to an inversion software relying on the Optimal Estimation Method, has been developed to retrieve HNO_3 total columns in near-real time. The resulting product has been thoroughly described here. Global distributions have been retrieved daily for a 10 months period starting from March 2008, providing an unprecedented view of the nitric acid fields and their seasonal and inter-hemispheric variations. Estimated errors on the total columns are found to be highly variable. We have shown that IASI measurements capture the hemispheric gradient from low values at the equator to higher values toward the poles. The amplitude of the seasonal variations is negligible at tropical latitudes and becomes pronounced at middle and polar latitudes. Overall, larger HNO_3 columns are measured in winter and spring polar regions and lower values are found in summertime, resulting from more active photochemistry. However, we have shown that daily variations of the total columns in small grid boxes are relatively important and partly mask the seasonal variations. Beside the general trends with season and latitude, the remarkable denitrification processes occurring in the winter polar region when temperatures are low enough to form PSCs have been observed in the Antarctic between June and December 2008. Polar

regions exhibit well the fact that the wintertime HNO_3 distributions are governed by the strength and the spatial extent of the polar vortex as well as by the lowest temperatures, which control the formation of PSC particles.

Overall, the trends observed are representative of stratospheric processes. Initial qualitative comparisons with MLS measurements of HNO_3 in a lower stratospheric layer at specific locations have been performed. The trends of total columns are in agreement with those of MLS mixing ratios in the stratosphere. The most remarkable gain of IASI lies in the number of measurements, which allows monitoring daily and small-scale spatial variations. A preliminary comparison between HNO_3 and O_3 distributions at high latitudes in the Southern Hemisphere has been conducted in order to illustrate the potential of IASI to contribute to in-depth analyses of chemical processes, such as those occurring in the Antarctic vortex. The distributions of HNO_3 and O_3 were compared for periods characterized by depletion of HNO_3 at polar latitudes. Time series of the HNO_3/O_3 ratios have been analyzed. On average, the ratios vary from 1×10^{-3} to 4×10^{-3} with minimum values in the severely denitrified region.

The results presented here open further perspectives. In particular, long-term time-series are expected, given the 15 years of the IASI program, which will allow an analysis of inter-annual variability. Furthermore, work is in progress to isolate the tropospheric HNO_3 contribution from the IASI spectra, through combination with other satellite instruments and data assimilation.

Acknowledgements. IASI has been developed and built under the responsibility of the Centre National d'Etudes Spatiales (CNES, France). It is flown onboard the Metop satellites as part of the EUMETSAT Polar System. The IASI L1 data are received through the EUMETCast near real time data distribution service. C. Wespes and P. F. Coheur are respectively FRIA Researcher and Research Associate with FRS-FNRS. The research was funded by the Fonds National de la Recherche Scientifique (FNRS, Belgium M.I.S. F.4511.08), the Belgian State Federal Office for Scientific, Technical and Cultural Affairs and the European Space Agency (ESA-Prodex arrangement C90-327). Financial support by FRIA and the "Communauté Française de Belgique-Actions de Recherche Concertées" are also acknowledged. Work at the Jet Propulsion Laboratory, California Institute of Technology, was done under contract with the National

Aeronautics and Space Administration.

References

Adams, P. J., Seinfeld, J. H., Koch, D. M., Mickley, L. J., and Jacob, D. J.: General circulation model assessment of direct radiative forcing by the sulfate-nitrate-ammonium-water inorganic aerosol system, J. Geophys. Res., 106, 1097–1111, 2001.

Austin, J., Garcia, R., Russel III, J., Solomon, S., and Tuck, A.: On the atmospheric photochemistry of nitric acid, J. Geophys. Res., 91, 5477–5484, 1986.

Barret, B., Turquety, S., Hurtmans, D., Clerbaux, C., Hadji-Lazaro, J., Bey, I., Auvray, M., and Coheur, P.-F.: Global carbon monoxide vertical distributions from spaceborne high-resolution FTIR nadir measurements, Atmos. Chem. Phys., 5, 2901–2914, 2005, http://www.atmos-chem-phys.net/5/2901/2005/.

Beer, R.: TES on the Aura Mission: Scientific Objectives, Measurements and Analysis Overview, IEEE T. Geosci. Remote Sens., 44, 1102–1105, 2006.

Bernath, P. F., McElroy, C. T., Abrams, M. C., Boone, C. D., Butler, M., Camy-Peyret, C., Carleer, M., Clerbaux, C., Coheur, P. F., Colin, R., DeCola, P., Bernath, P. F., McElroy, C. T., Abrams, M. C., Boone, C. D., Butler, M., Camy-Peyret, C., Carleer, M., Clerbaux, C., Coheur, P. F., Colin, R., DeCola, P., DeMaziere, M., Drummond, J. R., Dufour, D., Evans, W. F. J., Fast, H., Fussen, D., Gilbert, K., Jennings, D. E., Llewellyn, E. J., Lowe, R. P., Mahieu, E., McConnell, J. C., McHugh, M., McLeod, S. D., Michaud, R., Midwinter, C., Nassar, R., Nichitiu, F., Nowlan, C., Rinsland, C. P., Rochon, Y. J., Rowlands, N., Semeniuk, K., Simon, P., Skelton, R., Sloan, J. J., Soucy, M. A., Strong, K., Tremblay, P., Turnbull, D., Walker, K. A., Walkty, I., Wardle, D. A., Wehrle, V., Zander, R., and Zou, J.: Atmospheric Chemistry Experiment (ACE): Mission overview, Geophys. Res. Lett., 32, L15S01, doi:10.1029/2005GL022386, 2005.

Bey, I., Jacob, D. J., Logan, J. A., and Yantosca, R. M.: Asian chemical outflow to the Pacific in spring: Origins, pathways, and budgets, J. Geophys. Res., 106, 23097–23113, 2001.

Brasseur, G. and Solomon, S.: Aeronomy of the middle atmosphere: Chemistry and physics of 10 the stratosphere and mesosphere, 3. Edition, Springer, Dordrecht, The Netherlands, 2005.

Bregman, A., van Velthoven, P. F. J., Wienhold, F. G., Fischer, H., Zenker, T., Waibel, A., Fren-

zel, A., Arnold, F., Harris, G. W., Bolder, M. J. A., and Lelieveld, J.: Aircraft measurements of O_3, HNO_3, and N_2O in the winter Arctic lower stratosphere during the Stratosphere-Troposphere Experiment by Aircraft Measurements (STREAM) 1, J. Geophys. Res., 100, 11245–11260, 1995.

Boone, C. D., Nassar, R.,Walker, K. A., Rochon, Y., McLeod, S. D., Rinsland, C. P., and Bernath, P. F.: Retrievals for the atmospheric chemistry experiment Fourier-transform spectrometer, Appl. Optics, 44, 7218–7231, 2005.

Boynard, A., Clerbaux, C., Coheur, P.-F., Hurtmans, D., Turquety, S., George, M., Hadji-Lazaro, J., Keim, C., and Meyer-Arnek, J.: Measurements of total and tropospheric ozone from IASI: comparison with correlative satellite and ozonesonde observations,Atmos. Chem. Phys. Discuss., IASI Special Issue, submitted, 2009.

Clerbaux, C., Hadji-Lazaro, J., Turquety, S., George, M., Coheur, P. F., Hurtmans, D., Wespes, C., Herbin, H., Blumstein, D., Tournier, B., Phulpin, T.: The IASI/MetOp I mission: First observations and highlights of its Potential Contribution to GMES, COSPAR inf. Bul., vol. 2007, 19–24, 2007.

Clerbaux, C., Boynard, A., Clarisse, L., George, M., Hadji-Lazaro, J., Hurtmans, D., Herbin, H., Pommier, M., Razavi, A., Turquety, S., Wespes, C., and Coheur, P. F.: Monitoring of atmospheric composition using the thermal infrared IASI/METOP sounder, Atmos. Chem. Phys. Discuss., IASI Special Issue, accepted, 2009.

Clarisse, L., Coheur, P. F., Prata, A. J., Hurtmans, D., Razavi, A., Phulpin, T., Hadji-Lazaro, J., and Clerbaux, C.: Tracking and quantifying volcanic SO_2 with IASI, the September 2007 eruption at Jebel at Tair, Atmos. Chem. Phys., 8, 7723–7734, 2008, http://www.atmos-chem-phys.net/8/7723/2008/.

Coheur, P. F., Barret, B., Turquety, S., Hurtmans, D., Hadji-Lazaro, J., and Clerbaux, C.: Retrieval and characterization of ozone vertical profiles from a thermal infrared nadir sounder, J. Geophys. Res., 110, D24303, doi:24310.21029/22005JD005845, 2005.

Coheur P. F., Clarisse, L., Turquety, S., Hurtmans, D., and Clerbaux, C.: IASI measurements of reactive trace species in biomass burning plumes, Atmos. Chem. Phys. Discuss., submitted, IASI Special Issue, 2009.

Emmons, L. K., Hauglustaine, D. A., Müller, J. F., Carroll, M. A., Brasseur, G. P., Brunner, D., Staehelin, J., Thouret, V., and Marenco, A.: Data composites of airborne observations of tropospheric ozone and its precursors, J. Geophys. Res., 105, 20497–20538, 2000.

Fischer, H., Birk, M., Blom, C., Carli, B., Carlotti, M., von Clarmann, T., Delbouille, L., Dudhia,

A., Ehhalt, D., Endemann, M., Flaud, J. M., Gessner, R., Kleinert, A., Koopman, R., Langen, J., López-Puertas, M., Mosner, P., Nett, H., Oelhaf, H., Perron, G., Remedios, J., Ridolfi, M., Stiller, G., and Zander, R.: MIPAS: an instrument for atmospheric and climate research, Atmos. Chem. Phys., 8, 2151–2188, 2008, http://www.atmos-chem-phys.net/8/2151/2008/.

Froidevaux, L., Livesey, N. J., Read, W. G., Jiang, Y. B., Jimenez, C. J., Filipiak, M. J., Schwartz, M. J., Santee, M. L., Pumphrey, H. C., Jiang, J. H., Wu, D. L., Manney, G. L., Drouin, B. J., Waters, J. W., Fetzer, E. J., Bernath, P. F., Boone, C. D., Walker, K. A., Jucks, K. W., Toon, G. C., Margitan, J. J., Sen, B., Webster, C. R., Christensen, L. E., Elkins, J. W., Atlas, E., Lueb, R. A., and Hendershot, R.: Early validation analyses of atmospheric profiles from EOS MLS on the Aura satellite, IEEE T. Geosci. Remote Sens., 44(5), 1106–1121, 2006.

George, M., Clerbaux, C., Hurtmans, D., Turquety, S., Coheur, P.-F., Pommier, M., Hadji-Lazaro, J., Edwards, D., Worden, H., Luo, M., Rinsland, C. P., and McMillan, W.: Carbon monoxide distributions from the IASI/METOP mission: evaluation with other spaceborne remote sensors, Atmos. Chem. Phys. Discuss., IASI Special Issue, accepted, 2009.

Hauglustaine, D. A., Brasseur, G. P., Walters, S., Rasch, P. J., Müller, J.-F., Emmons, L. K., and Carroll, M. A.: MOZART, a global chemical transport model for ozone and related chemical tracers, J. Geophys. Res., 103, 28291–28335, 1998.

Hauglustaine, D. A., Hourdin, F., Jourdain, L., Filiberti, M. A., Walters, S., Lamarque, J. F., and Holland, E. A.: Interactive chemistry in the laboratoire de meteorologie dynamique general circulation model: Description and background tropospheric chemistry evaluation, J. Geophys. Res.-Atmos., 109, D04314, doi:10.1029/2003JD003957, 2004.

Hudman, R. C., Jacob, D. J., Cooper, O. R., Evans, M. J., Heald, C. L., Park, R. J., Fehsenfeld, F., Flocke, F., Holloway, J., Hübler, G., Kita, K., Koike, M., Kondo, Y., Neuman, A., Oltmans S., Parrish, D., Robert, J. M., and Ryerson, T.: Ozone production in transpacific Asian pollution plumes and implications for ozone air quality in California, J. Geophys. Res., 109, D23S10, doi:10.1029/2004JD004974, 2004.

Irie, H., Kondo, Y., Koike, M., Danilin, M. Y., Camy-Peyret, C., Payan, S., Pommereau, J. P., Goutail, F., Renard, J.-B., Oelhaf, H., Wetzel, G., Toon, G. C., Sen, B., Blavier, J.-F., Salawitch, R., Bevilacqua, R. M., Russell J. M., Kanzawa, H., Nakajima, H., Yokota, Y., Sugita, T., and Sasano, Y.: Validation of NO_2 and HNO_3 measurements from the Improved Limb Atmospheric Spectrometer (ILAS) with the version 5.20 retrieval algorithm, J. Geophys. Res., 107, D248206, doi:10.1029/2001JD001304, 2002.

Irie, H., Sugita, T., Nakajima, H., Yokota, T., Oelhaf, H., Wetzel, G., Toon, G. C., Sen, B., Santee, M. L., Terao, Y., Saitoh, N., Ejiri, M. K., Tanaka, T., Kondo, Y., Kanzawa, H., Kobayashi, H., and Sasano, Y.: Validation of stratospheric nitric acid profiles observed by Improved Limb Atmospheric Spectrometer (ILAS-II), J. Geophys. Res., 111, D11S03, doi:10.1029/2005JD006115, 2006.

Jin, J. J., Semeniuk, K., Manney, G. L., Jonsson, A. I., Beagley, S. R., McConnell, J. C., Rinsland, C. P., Boone, C. D., Walker, K. A., Bernath, P. F.: Denitrification in the Arctic winter 2004/2005: Observation from ACE-FTS, Geophys. Res. Lett., 33, L19814, doi:10.1029/2006GL027687, 2006.

Koike, M., Kondo, Y., Irie, H., Murcray, F. J., Williams, J., Fogal, P., Blatherwick, R., Camy-Peyret, C., Payan, S., Oelhaf, H., Wetzel, G., Traub, W., Johnson D., Jucks K., Toon, G. C., Sen, B., Blavier, J.-F., Schlager, H., Ziereis, H., Toriyama, N., Danilin, M. Y., Rodriguez, J. M., Kanzawa, H., and Sasano Y.: A comparison of Arctic HNO_3 profiles measured by the Improved Limb Atmospheric Spectrometer and balloon-borne sensors, J. Geophys. Res., 105, 6761–6771, 2000.

Massart, S., Clerbaux, C., Cariolle, D., Piacentini, A., Turquety, S., and Hadji-Lazaro, J.: First steps towards the assimilation of IASI ozone data into the MOCAGE-PALM system, Atmos. Chem. Phys. Discuss., 9, 6691–6737, 2009, http://www.atmos-chem-phys-discuss.net/9/6691/2009/.

Martin, R. V., Sauvage, B., Folkins, I., Sioris, C. E., Boone, C., Bernath, P., and Ziemke, J.: Space-based constraints on the production of nitric oxide by lightning, J. Geophys. Res., 112, D09309, doi:10.1029/2006JD007831, 2006.

Miyazaki, Y., Koike, Y., Fuelberg, H. E., Kiley, C. M., Kita, K., Takegawa, N., Sachse, G. W., Flocke, F., Weinheimer, A. J., Singh, H. B., Eisele, F. L., Zondlo, M., Talbot, R. W, Sandholm, S. T., Avery, M. A., and Blake, D. R.: Synoptic-scale transport of reactive nitrogen over the western Pacific in spring, J. Geophys. Res., 108, D208788, doi:10.1029/2002JD003248, 2003.

Neuman, J. A., Gao, R. S., Fahey, D. W., Holecek, J. C., Ridley, B. A., Walega, J. G., Grahek, F. E., Richard, E. C., McElroy, C. T., Thompson, T. L., Elkins, J. W., Moore, F. L., and Ray, E. A.: In situ measurements of HNO_3, NO_y, NO, and O_3 in the lower stratosphere and upper troposphere, Atmos. Environ., 35, 5789–5797, 2001.

Neuman, J. A., Parrish, D. D., Trainer, M., Ryerson, T. B., Holloway, J. S., Nowak, J. B., Swanson, A., Flocke, F., Roberts, J. M., Brown, S. S., Stark, H., Sommariva, R., Stohl, A., Peltier,

R., Weber, R., Wollny, A. G., Sueper, D. T., Hubler, G., and Fehsenfeld, F. C.: Reactive nitrogen transport and photochemistry in urban plumes over the North Atlantic Ocean, J. Geophys. Res., 111, D23S54, doi:10.1029/2005JD007010, 2006.

Razavi, A., Clerbaux, C., Wespes, C., Clarisse, L., Hurtmans, D., Payan, S., Camy-Peyret, C., and Coheur, P. F.: Characterization of methane retrievals from the IASI space-borne sounder, Atmos. Chem. Phys. Discuss., IASI Special Issue, in press, 2009.

Rinsland, C. P., Zander, R., and Demoulin, P.: Ground-based infrared measurements of HNO_3 total column abundances: Long-term trend and variability, J. Geophys. Res., 96, 9379–9389, 1991.

Rodgers, C. D.: Inverse methods for atmospheric sounding: Theory and Practice, World Sci., River Edge, NJ, USA, 2000.

Rothman, L. S., Jacquemart, D., Barbe, A., Chris Benner, D., Birk, M., Brown, L. R., Carleer, M. R., Chackerian Jr., C., Chance, K., Coudert, L. H., Dana, V., Devi, V. M., Flaud, J.-M., Gamache, R. R., Goldman, A., Hartmann, J.-M., Jucks, K. W., Maki, A. G., Mandin, J.-Y, Massie, S. T., Orphal, J., Perrin, A., Rinsland, C. P., Smith, M. A. H., Tennyson, J., Tolchenov, R. N., Toth, R. A., Vander Auwera, J., Varanasi, P., and Wagner, G.: The HITRAN 2004 molecular spectroscopic database, J. Quant. Spectrosc. Ra. Transfer, 96, 139–204, 2005.

Santee, M. L., Manney, G. L., Froidevaux, L., Read, W. G., and Waters, J. W.: Six years of UARS Microwave Limb Sounder HNO_3 observations: Seasonal, interhemispheric, and interannual variations in the lower stratosphere, J. Geophys. Res., 104, 8225–8246, 1999.

Santee, M. L., Manney, G. L., Livesey, N. J., and Read, W. G.: Three-dimensional structure and evolution of stratospheric HNO_3 based on UARS Microwave Limb Sounder measurements, J. Geophys. Res., 109, D15306, doi:10.1029/2004JD004578, 2004.

Santee, M. L., Manney, G. L., Livesey, N. J., Froidevaux, L., Pumphrey, H. C., Read, W. G., Schwartz, M. J., and Waters, J. W.: Polar processing and development of the 2004 Antarctic ozone hole: First results from Aura MLS, J. Geophys. Res., 32, L12817, doi:10.1029/2005GL022582, 2005.

Santee, M. L., Lambert, A., Read, W. G., Livesey, N. J., Cofield, R. E., Cuddy, D. T., Daffer, W. H., Drouin, B. J., Froidevaux, L., Fuller, R. A., Jarnot, R. F., Knosp, B. W., Manney, G. L., Perun, V. S., Snyder, W. V., Stek, P. C., Thurstans, R. P., Wagner, P. A., Waters, J. W., Muscari, G., de Zafra, R. L., Dibb, J. E., Fahey, D. W., Popp, P. J., Marcy, T. P., Jucks, K. W., Toon, G. C., Stachnik, R. A., Bernath, 5 P. F., Boone, C. D., Walker, K. A., Urban, J., and Murtagh, D.: Validation of the Aura Microwave Limb Sounder HNO_3 Measurements, J.

Geophys. Res., 112, D24S40, doi:10.1029/2007JD008721, 2007.
Schlüssel, P., Hultberg, T. H., Philipps, P. L., August, T., and Calbet, X.: The operational IASI Level 2 processor, Adv. Space Res., 36, 982–988, doi:10.1016/j.asr.2005.03.008, 2005.
Schneider J., Arnold, F., Curtius, J., Sierau, B., Fischer, H., Hoor, P., Wienhold, F. G., Parchatka, U., Zhang, Y. C., Schlager, H., Ziereis, H., Feigl, Ch., Lelieveld, J., Scheeren, H. A., and Bujok, O.: The temporal evolution of the ratio HNO_3/NO_y in the Arctic lower stratosphere from January to March 1997, Geophys. Res. Lett, 26(8), 1125–1128, 1999.
Stiller, G. P., Tsidu, G. M., von Clarmann, T., Glatthor, N., Höpfner, M., Kellmann, S., Linden, A., Ruhnke, R., and Fischer, H.: An enhanced HNO_3 second maximum in the Antarctic mid-winter upper stratosphere 2003, J. Geophys. Res., 110, D20303, doi:10.1029/2005JD006011, 2005.
Solomon, S.: Stratospheric Ozone Depletion: A review of concepts and history, Rev. Geophys., 37, 275–316, 1999.
Talbot, R. W., Dibb, J. E., Scheuer, E. M., Kondo, Y., Koike, M., Singh, H. B., Salas, L. B., Fukui, Y., Ballenthin, J. O., Meads, R. F., Miller, T. M., Hunton, D. E., Viggiano, A. A, Blake, D. R., Blake, N. J., Atlas, E., Flocke, F., Jacob, D. J., and Jeagle, L.: Reactive Nitrogen Budget During the NASA SONEX Mission, Geophys. Res. Lett., 26(20), 3057–3060, 1997.
Trainer, M., Parrish, D. D., Buhr, M. P., Norton, R. B., Fehsenfeld, F. C., Anlauf, K. G., Bottenheim, J. W., Tang, Y. Z., Wiebe, H. A., Roberts, J. M., Tanner, R. L., Newman, L., Bowersox, V. C., Meagher, J. F., Olszyna, K. J., Rodgers, M. O., Wang, T., Berresheim, H., Demerjian, K. L., and Roychowdhury, U. K.: Correlation of ozone with NO_y in photochemically aged air, J. Geophys. Res., 98, 2917–2925, 1993.
Tsidu, G. M., Stiller, G. P., von Clarmann, T., Funke, B., Hopfner, M., Fischer, H., Glatthor, N., Grabowski, U., Kellmann, S., Kiefer, M., Linden, A., Lopez-Puertas, M., Milz, M., Steck, T., and Wang, D. Y.: NO_y from Michelson Interferometer for Passive Atmospheric Sounding on Environmental Satellite during the Southern Hemisphere polar vortex split in September/October 2002, J. Geophys. Res., 110, D11301, doi:10.1029/2004JD005322, 2005.
Turquety, S., Hadji-Lazaro, J., Clerbaux, C., Hauglustaine, D. A., Clough, S. A., Casse, V., Schlüssel, P., and Mégie, G.: Operational trace gas retrieval algorithm for the Infrared Atmospheric Sounding Interferometer, J. Geophys. Res., 109, D21301, doi:21310.21029/22004JD00482, 2004.
Turquety, S., Hurtmans, D., Hadji-Lazaro, J., Coheur, P.-F., Clerbaux, C., Josset, D., and Tsamalis, C.: Tracking the emission and transport of pollution from wildfires using the IASI

CO retrievals: analysis of the summer 2007 Greek fires, Atmos. Chem. Phys. Discuss., IASI Special Issue, accepted, 2009.

Urban, J., Lautie, N., Le Flochmoën, E., Jimenez, C., Eriksson, P., de La Noe, J., Dupuy, E., Ekstrom, M., Amraoui, L. E., Frisk, U., Murtagh, D., Olberg, M., and Ricaud, P.: Odin/SMR limb observations of stratospheric trace gases: Level 2 processing of ClO, N_2O, HNO_3, and O_3, J. Geophys. Res., 110, D14307, doi:10.1029/2004JD005741, 2005.

Urban, J., Pommier, M., Murtagh, D. P., Santee, M. L., and Orsolini, Y. J.: Nitric acid in the stratosphere based on Odin observations from 2001 to 2007 – Part 1: A global climatology, Atmos. Chem. Phys. Discuss., 8, 9569–9590, 2008, http://www.atmos-chem-phys-discuss.net/8/9569/2008/.

Vigouroux, C., De Maziére, M., Errera, Q., Chabrillat, S., Mahieu, E., Duchatelet, P., Wood, S., Smale, D., Mikuteit, S., Blumenstock, T., Hase, F., and Jones, N.: Comparisons between ground-based FTIR and MIPAS N_2O and HNO_3 profiles before and after assimilation in BASCOE, Atmos. Chem. Phys., 7, 377–396, 2007, http://www.atmos-chem-phys.net/7/377/2007/.

Wang, D. Y., Höpfner, M., Blom, C. E., Ward, W. E., Fischer, H., Blumenstock, T., Hase, F., Keim, C., Liu, G. Y., Mikuteit, S., Oelhaf, H., Wetzel, G., Cortesi, U., Mencaraglia, F., Bianchini, G., Redaelli, G., Pirre, M., Catoire, V., Huret, N., Vigouroux, C., De Maziére, M., Mahieu, E., Demoulin, P., Wood, S., Smale, D., Jones, N., Nakajima, H., Sugita, T., Urban, J., Murtagh, D., Boone, C. D., Bernath, P. F., Walker, K. A., Kuttippurath, J., Kleinböhl, A., Toon, G., and Piccolo, C.: Validation of MIPAS HNO3 operational data, Atmos. Chem. Phys., 7, 4905–4934, 2007, http://www.atmos-chem-phys.net/7/4905/2007/.

Wespes, C., Hurtmans, D., Herbin, H., Barret, B., Turquety, S., Hadji-Lazaro, J., Clerbaux, C., and Coheur, P. F.: First global distributions of nitric acid in the troposphere and the stratosphere derived from infrared satellite measurements, J. Geophys. Res., 112, D13311, doi:10.1029/2006JD008202, 2007.

Wolff, M. A., Kerzenmacher, T., Strong, K., Walker, K. A., Toohey, M., Dupuy, E., Bernath, P. F., Boone, C. D., Brohede, S., Catoire, V., von Clarmann, T., Coffey, M., Daffer, W. H., De Maziére, M., Duchatelet, P., Glatthor, N., Griffith, D. W. T., Hannigan, J., Hase, F., Höpfner, M., Huret, N., Jones, N., Jucks, K., Kagawa, A., Kasai, Y., Kramer, I., Küllmann, H., Kuttippurath, J., Mahieu, E., Manney, G., McElroy, C. T., McLinden, C., Mébarki, Y., Mikuteit, S., Murtagh, D., Piccolo, C., Raspollini, P., Ridolfi, M., Ruhnke, R., Santee, M., Senten, C.,

Smale, D., Tétard, C., Urban, J., and Wood, S.: Validation of HNO_3, $ClONO_2$, and N_2O_5 from the Atmospheric Chemistry Experiment Fourier Transform Spectrometer (ACE-FTS), Atmos. Chem. Phys., 8, 3529–3562, 2008, http://www.atmos-chem-phys.net/8/3529/2008/.

Table 1. Retrieval settings applied for the operational retrievals of HNO_3 total columns using the FORLI-HNO_3 software.

Spectral range	860–900 cm^{-1}
x_a	LMDz-INCA (ground −15.6 km)/ACE (6.5–60.5 km) profile
S_a	100%
σ_ε	2×10^{-6} $W/(cm^2.sr.m^{-1})$
State vector	HNO_3 total column, Surface temperature, Water vapor profile from the ground to 19 km every km

Table 2. Selection of successive days within each month from March to December 2008, used to draw the zonal distributions of Fig. 4.

Months	Selected days
March	1–7
April	9–15
May	9–15
June	10–13
July	9–15
August	8–10
September	6–9
October	14–20
November	9–15
December	17–23

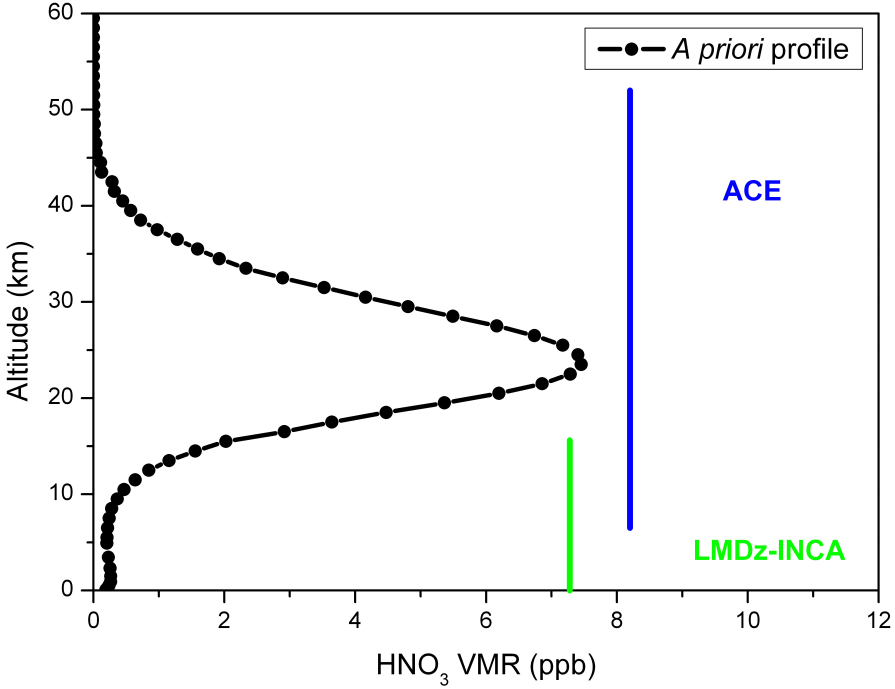

Fig. 1. Global HNO_3 a priori profile (black line) constructed from one year of modeled LMDz-INCA profiles from the ground to 15.6 km (delimited by the green line) and from two years of measured ACE profiles from 6.5 to 60.5 km (delimited by the blue line).

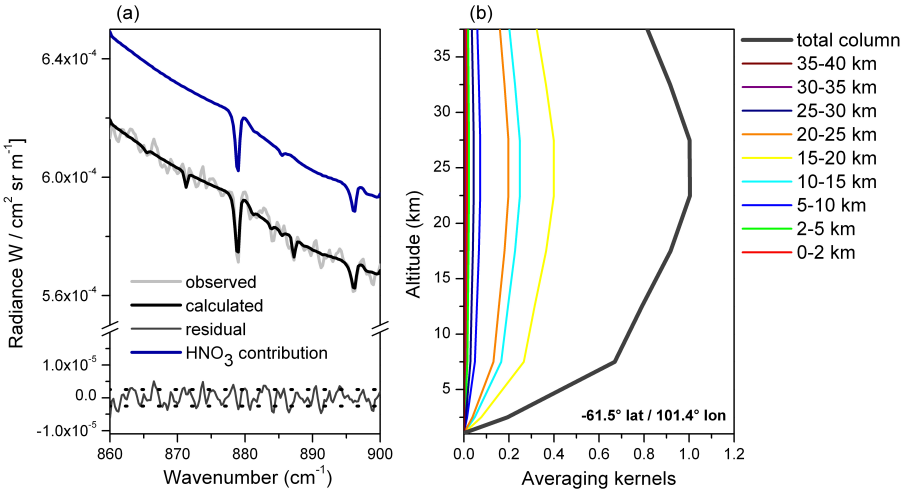

Fig. 2. Left: example of a spectral fit for one typical IASI measurement at polar latitude. The light grey and the black lines represent the observed and HNO_3 fitted spectra, respectively. The dark grey line is the adjusted HNO_3 contribution and is shifted on the vertical scale for clarity. The residual (observed-fitted spectra), with associated RMS is also shown in comparison with the σ_ε value selected (2×10^{-6} W/(cm^2.sr.m^{-1})) for the retrievals (dashed horizontal lines). Right: averaging kernels for this particular retrieval, in partial column units, for nine retrieved layers and for the total column (black).

ACPD
9, 8035–8069, 2009

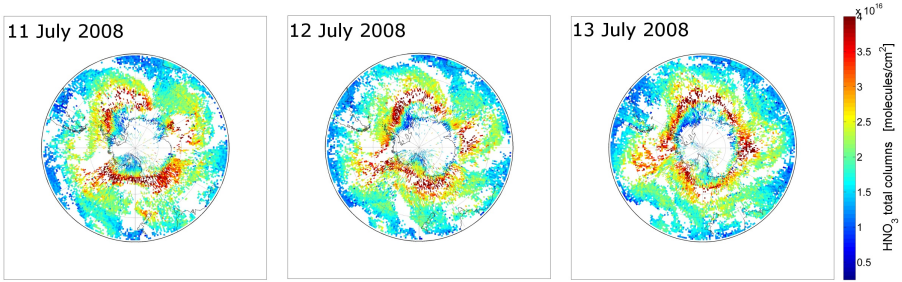

Fig. 3. Antarctic projections of IASI HNO_3 total columns retrieved from FORLI near-real-time processing for three successive days in July 2008. Data have been gridded on 1°×1°. White areas result from the applied filters (Sect. 2.4).

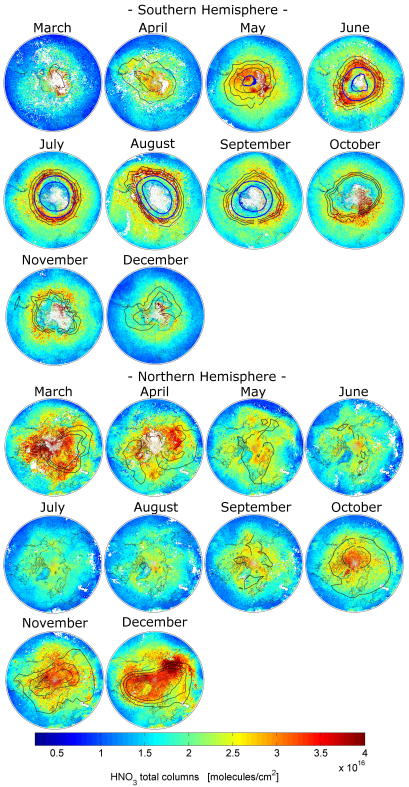

Fig. 4. Polar projections of IASI HNO_3 total columns for the Southern Hemisphere (top) and the Northern Hemisphere (bottom). Data are gridded on 1°×1° by averaging selected days within each month from March to December 2008 (see Table 2). Three contours of Met Office potential vorticity at a potential temperature of 520 K are superimposed as black lines. The -0.60×10^{-4} K.m^2.kg^{-1}.s^{-1} contour represents approximately the edge of the Antarctic winter polar vortex at this level. Other contours have been added ($+/-0.50\times10^{-4}$ K.m^2.kg^{-1}.s^{-1} and $+/-0.40\times10^{-4}$ K.m^2.kg^{-1}.s^{-1}) to evaluate the size and the strength of the polar vortex. The contours of 195 K, 188 K temperature at 50 hPa (~25 km) taken from Eumetcast level 2 data are also indicated by blue lines for the concerned months.

ACPD
9, 8035–8069, 2009

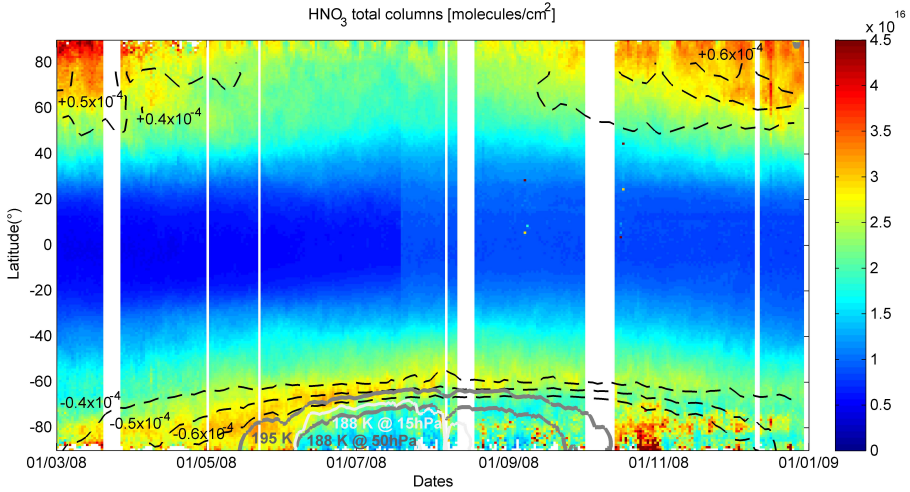

Fig. 5. Time series of IASI HNO_3 total columns (molecules.cm^{-2}) as a function of latitude, obtained by averaging data on a 1 day×1° grid. The isocontours of 195 K, 188 K for temperature at 50 (grey lines) and 15 hPa (white line) (~20 and 25 km) taken from Eumetcast level 2 data are plotted along with three different contours of potential vorticity as in Fig. 4.

ACPD
9, 8035–8069, 2009

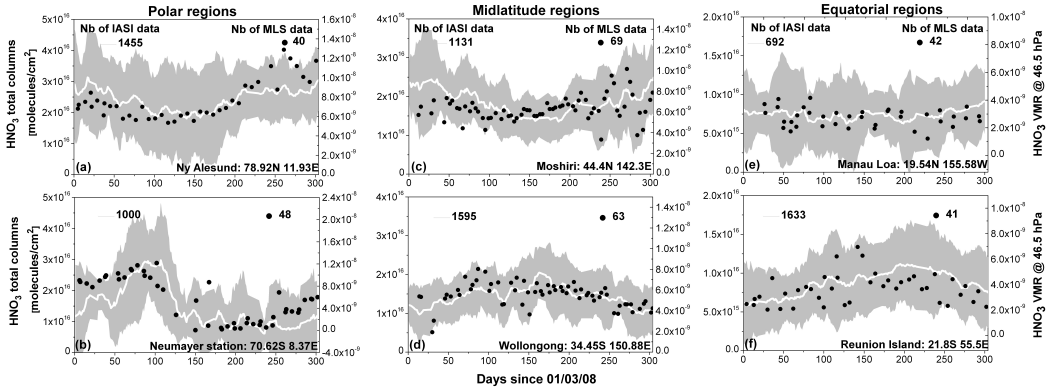

Fig. 6. Time series of IASI HNO_3 total columns for 1° latitude × 2° longitude area around six selected NDACC (Network for the Detection of Atmospheric Composition Change) stations in polar **(a, b)**, midlatitude **(c, d)** and equatorial **(e, f)** regions. The daily average trend is shown as a white line. The grey area represents 3σ, where σ is the standard deviation around the daily average within the grid box. HNO_3 volume mixing ratios at 46.5 hPa (~25 km) (right axis) retrieved from co-located MLS/Aura are superposed for a sake of comparison.

ACPD
9, 8035–8069, 2009

Title Page
Abstract | Introduction
Conclusions | References
Tables | Figures
◄◄ | ►►
◄ | ►
Back | Close
Full Screen / Esc
Printer-friendly Version
Interactive Discussion

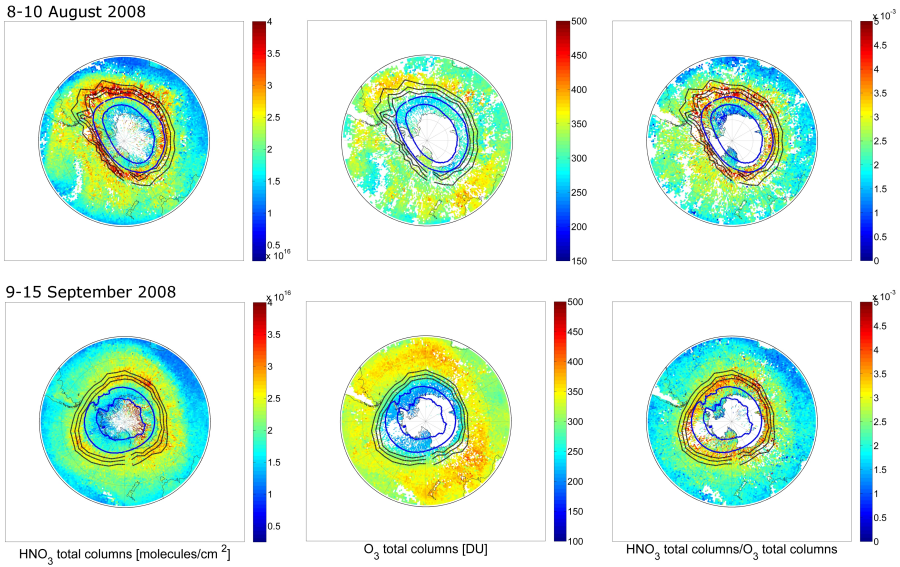

Fig. 7. Southern Hemispheric polar projections of IASI HNO_3, O_3 total columns and HNO_3/O_3 ratios for two periods characterized by depletion of HNO_3 and/or O_3. As in plate 4, contours of Met Office potential vorticity at a potential temperature of 520 K and temperature contours of 195 and 188 K at 50 hPa are shown.

ACPD
9, 8035–8069, 2009

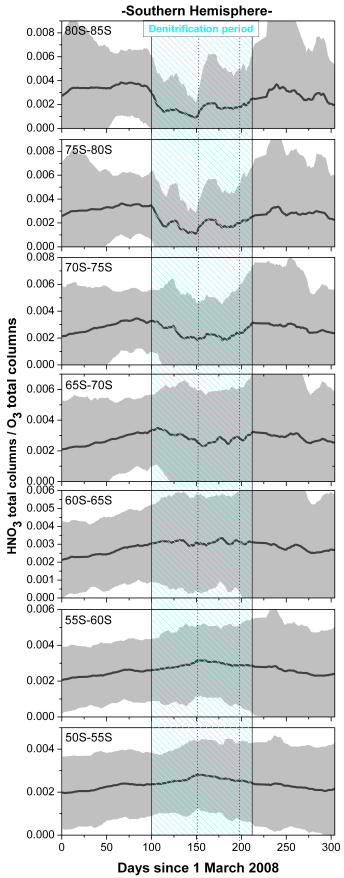

Fig. 8. Time series of HNO_3/O_3 total column ratio for 7 latitude bands in the Southern Hemisphere. The daily average trend of the ratio is shown as a black line. The grey area represents 3σ where σ is the standard deviation around the average. The blue area defines the period of strong denitrification. The two dashed lines inside this blue area highlight the period selected for Plate 7.